

## Sensor and Simulation Notes

Note 530

December 2007

### Rigorous Analysis of an Impulse Radiating Antenna with a Non-ideal Feed Structure

James McLean and Robert Sutton

TDK R& D Corp.

1101 Cypress Creek Road

Cedar Park, Texas 78613

#### **Abstract**

The 4:1 equal-delay transformer/balun integral to some impulse radiating antenna (IRA) designs is analyzed including the effects of non-commensurate constituent transmission lines. Specifically, we develop a 2-port Thévenin equivalent source representation of the feed structure that is compatible with most numerical simulations. It is shown that the non-commensurate nature of the balun manifests itself in quasi-periodic frequency-domain ripple in the power transfer of the balun as well as excitation of the common mode. A representative, practical IRA is analyzed by combining the analytically-derived 2-port Thévenin equivalent source with a commercial finite element analysis in order to include many details of the radiating structure. Despite the anomalous behavior of the non-commensurate balun, the impulse radiating antenna is shown to produce almost no significant common mode radiation even when the electrical lengths of the constituent transmission lines are significantly non-commensurate.

# 1 Introduction

The Impulse Radiating Antenna (IRA) [1] has been proven to be very useful in radiating and receiving fast-rise-time impulses. The antenna employs a reflector and a unique, terminated Transverse-ElectroMagnetic (TEM) feed structure which, in principle, provides a distortionless transfer function. The overall reflector/feed system then produces a radiated impulse on its principal axis that is proportional to the time-derivative of the input time-domain voltage waveform. Finally, the PxM nature of the feed system provides a unidirectional pattern well below the efficient operating frequency range of the reflector and produces an electromagnetic field that exhibits a ratio of transverse electric to magnetic components nearly equal to that of a plane wave even in its near field region [2]. Thus, the IRA is an excellent candidate for some electromagnetic susceptibility testing applications. Because of the inherent impedance level of the system, that is, the characteristic impedance of the self-complementary transmission line feed, and the balanced nature of the antenna, it is advantageous to employ an impedance transformer to transform from 50 Ohms to 200 Ohms. Also, due to the balanced nature of the system, some sort of balancing network (balun) must be employed. Thus, a very commonly-used feed network topology intrinsically contains a 4:1 (impedance transformation) equal-delay or Guanella balun [3] as described in [4] and shown schematically in Fig. 2. The constituent transmission lines in this balun are necessarily electrically long over most of the operating frequency range of the antenna. As was shown in [5], when the electrical lengths of the two constituent transmission lines are not commensurate, anomalies in the response occur at odd-integer multiples of the average quarter-wave frequency of the two constituent lines. These anomalies involve undulations in the power transfer, peaks in the return loss of the system, and excitation of the common mode of the radiating structure. Because of the extremely broad operating frequency range of such an antenna, many such anomalies should manifest themselves in the antenna's response. Here we present a rigorous approach for the modeling of the non-ideal balun as well as details of the anomalous behavior. Finally, we examine the response of a commercially-produced IRA for such anomalies. Although feed structures for IRAs have been presented elsewhere [4], we believe this is the first such detailed analysis of the feed structure and its impact on the performance of the IRA. This note includes material originally presented at the EMC Zürich 2007 Symposium in München. in ref. [6].

The practical IRA considered here is, to the extent possible, based on the Farr Research model IRA-3M. This IRA has a reflector diameter of 18 inches and an  $F/D$  ratio of .5. A solid model of the antenna used in the finite element simulation is given in Fig. 1 which also shows the coordinate system used throughout this note. In this coordinate system, the

$z$  axis is taken as the bore-sight direction and the co-polarization direction on the principal axis is taken as the  $x$ -direction.

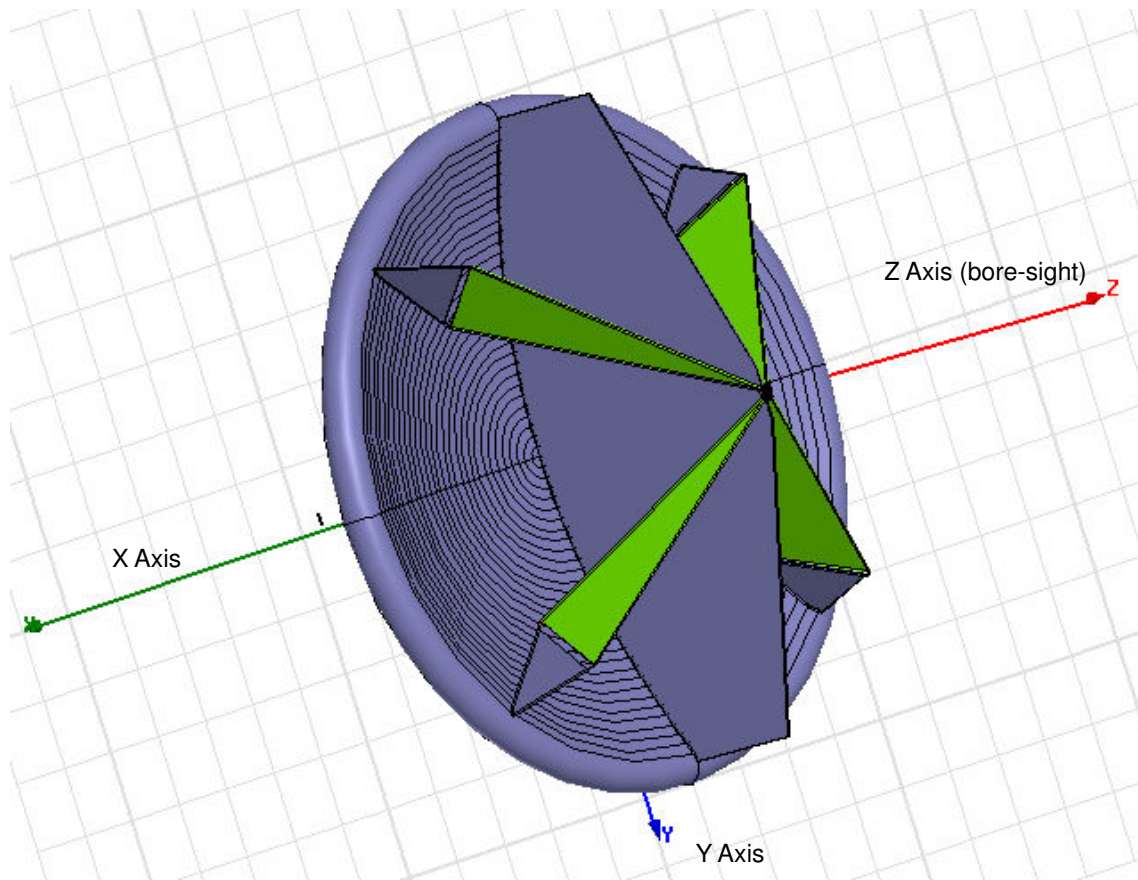


Figure 1: Solid model representing the Farr Research model IRA-3M.

## 2 Model for Feed Network

### 2.1 Equal-delay Balun/Transformer

The equal-delay topology provides a convenient, broadband, 4:1 impedance transformation as well as balancing action. With perfectly efficacious choking action, and absent any parasitic mechanisms, such a balun is, in some regards, truly frequency independent [3]. Nevertheless, this component of the IRA is one of the principal sources of non-ideal behavior. As shown in Fig. 3, this topology consists of the parallel-series connection of two constituent transmission lines for which the common mode of each line has been effectively choked off. In practice the common mode cannot be completely choked off. For an electrically-large transformer, the common mode can radiate, as is the case with the

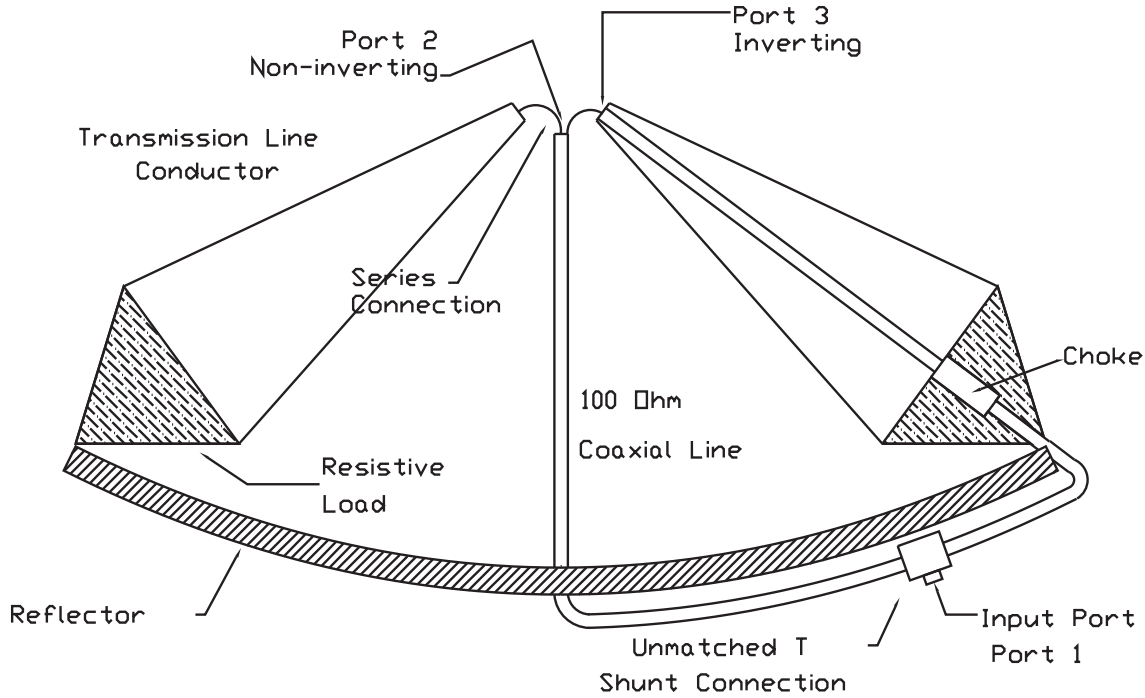


Figure 2: Schematic drawing of feed structure for IRA incorporating 4:1 impedance transforming balun.

feed of an IRA. As was shown in ref. [7], a 2-port, 3-terminal load such as a Y/T or  $\Pi/\Delta$  network is the appropriate network model for the radiating portion of the IRA. In Fig. 3, such a generalized 2-port, 3-terminal load is shown. As discussed in [7], the load representing an antenna is, in general, asymmetric. For the purpose of discussion, we assume the IRA is symmetric with  $Y_A^\Delta = Y_C^\Delta$ . The differential-mode (DM) admittance of the load,  $Y_{DM} = Y_B + \left(\frac{1}{Y_A^\Delta} + \frac{1}{Y_C^\Delta}\right)^{-1}$ , represents the IRA feed driven in the differential mode. The common-mode (CM) admittance,  $Y_{CM} = Y_A^\Delta + Y_C^\Delta$ , is the admittance seen by driving all four feed arms together against the center plate (if there is no center plate, against the shield of the center coaxial feed line) and reflector.

In [5], an idealized equal-delay transformer was examined in order to show how the anomalies occur. It was noted that these fluctuations are exacerbated, perhaps counter-intuitively, by increased CM impedance. In the ideal case of infinite CM impedance and an isolated load ( $Y_A^\Delta = Y_C^\Delta = 0$ ), they manifest themselves as transmission zeros of the system. That is, at odd integer multiples of the average quarter-wave frequency, the system will not transmit at all. In the case of the IRA, the CM impedance is not necessarily high and the load cannot be represented by an isolated, 2-terminal impedance. This case is intermediate and the CM structure is complicated. It was also shown in [5] that connection of the terminal labeled sum (because it is the sum port of the hybrid) is central to the

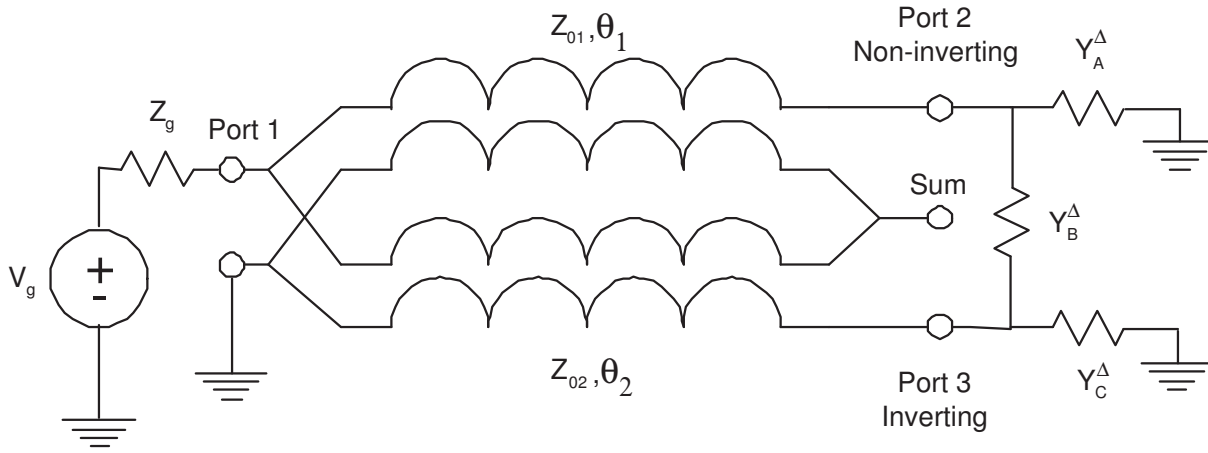


Figure 3: Guanella 4:1 impedance transformer with generalized load. The sum port is equivalent to the sum port of the hybrid described in [3].

behavior of the non-commensurate transformer.

In such an impedance transformer or balun, it is necessary to transpose the conductors of one of the constituent transmission lines at one end of the transformer or the other. That is, one of the constituent transmission lines must serve as a phase inverter. Thus, if the unit is implemented with coaxial cables, the shield must be broken at one end of the transformer or the other. In [8] a more typical coaxial implementation of this transformer is given with the shield broken on the low impedance side. In the IRA, the parallel connection of transmission lines is implemented with a simple shielded unmatched “T” connection. That is, a 50 Ohm coaxial cable splits into two 100 Ohm cables in parallel. Thus, up to the point at which the series connection is made, this transformer is simply the unmatched T with two nominally commensurate coaxial transmission lines attached. Therefore, with absolutely no loss in rigor, at least this much of the overall system can be modeled as a 2-port Thévenin source.

A central assumption in this analysis is that the feed region is electrically small and current continuity can be assumed for each connection. This assumption is reasonable in that the lengths of the feed transmission lines are long and retardation in the feed structure will manifest itself well before the finite size of the feed region (the region of the series connection) does. In order for the Thévenin source representation to be sound, it is necessary to unequivocally define the reference node. Here it is taken as the point at which the break in the shield of the center coaxial feed line is made and also where the center conductor of the other coaxial feed line is attached to the H-plane symmetry plate. When the feed region is electrically small, the transposition of conductors can be modeled as an ideal 1:1, phase-inverting transformer. This, in turn, can be absorbed into the 2-port model by invert-

ing one of the two independent sources and the sign of the transfer impedance. This affects all three of the passive impedances in the Thévenin equivalent source. We emphasize that the principal assumption here is that Kirchoff's current law holds in the feed region. *All of the characteristics of the CM structure are thus included as part of the external problem.*

## **2.2 The Generalized Thévenin Equivalent Network**

When there is a clear break in the system such that the non-radiating and radiating portions of the system can be separated, it is useful and possible to represent the non-radiating portion of the system with an equivalent Thévenin or Norton source. This simplifies the numerical modeling of the system in that the shielded part of the feed network need not be simulated simultaneously with the radiating structure. Furthermore, it also provides some physical insight into the operation and limitations of this system. The existence of such a 2-port equivalent source was proven in [9], where a general derivation technique was presented. The use of such an equivalent source with so-called "calculable" dipole antennas has been examined in some detail in [10]. We note here that because of the shunt connection at the splitter, the equivalent 2-port source cannot consist of two uncoupled independent voltage sources. Coupling between the sources must be included in the model. It is this coupling combined with non-commensurate transmission line lengths that causes the anomalous behavior. The Thévenin equivalent network is shown in [9] to consist of a passive 2-port network with two independent voltage sources in series at its two ports as shown in Fig. 4. The passive 2-port network is obtained by shorting the independent voltage source at the input of the shunt splitter, retaining, of course, the source impedance. Note that any length of intervening coaxial line between the source and the shunt splitter serves only to provide an overall phase shift to the independent sources in the Thévenin equivalent model; only the lengths of the transmission lines between the splitter and the antenna feed point affect the performance of the system. If we were to consider only this shunt splitter and coaxial transmission lines without the transposition, the 2-port impedance

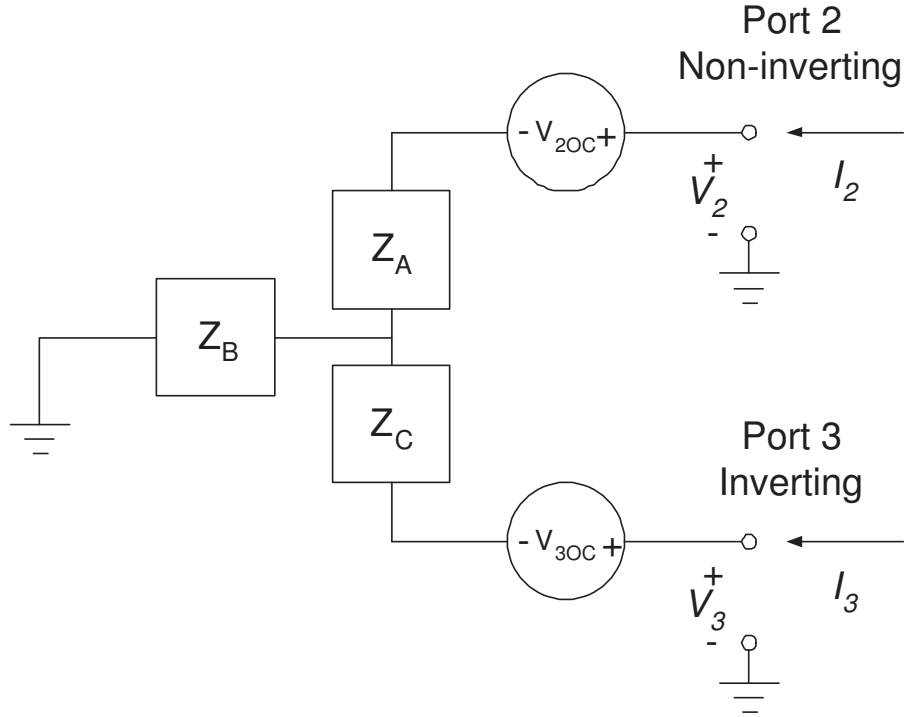


Figure 4: Thévenin Equivalent Model for 3-port consisting of unmatched splitter and 100-Ohm coaxial transmission lines. The “ground” symbol in this schematic indicates a single point or reference node, the point in Fig. 3 at which the center conductor of the coaxial line labeled as 2 (inverting) connects to the shield of the coaxial line labeled 1 (non-inverting). In Fig. 2, this is where the center conductor of the coaxial line on the right connects to the shield of the center coaxial line parallel to the bore-sight direction. Essentially, this implements the series connection of the two coaxial lines.

representation would be:

$$Z'_{22} = Z_{01} \frac{Y_{01} - Y_{02} \tan \theta_1 \tan \theta_2 + jY_g \tan \theta_1}{Y_g + jY_{02} \tan \theta_2 + jY_{01} \tan \theta_1} \quad (1)$$

$$Z'_{33} = Z_{02} \frac{Y_{02} - Y_{01} \tan \theta_2 \tan \theta_1 + jY_g \tan \theta_2}{Y_g + jY_{01} \tan \theta_1 + jY_{02} \tan \theta_2} \quad (2)$$

$$\begin{aligned} Z'_{23} &= Z'_{32} \\ &= \frac{1}{jY_{01} \sin \theta_1 \cos \theta_2 + Y_g \cos \theta_1 \cos \theta_2 + jY_{02} \cos \theta_1 \sin \theta_2} \\ &= \frac{\sec \theta_1 \sec \theta_2}{Y_g + jY_{01} \tan \theta_1 + jY_{02} \tan \theta_2}, \end{aligned} \quad (3)$$

where the prime notation indicates that these parameters apply to the shunt splitter without the transposition. Now, with a 1:1, ideal, phase-inverting transformer inserted between port

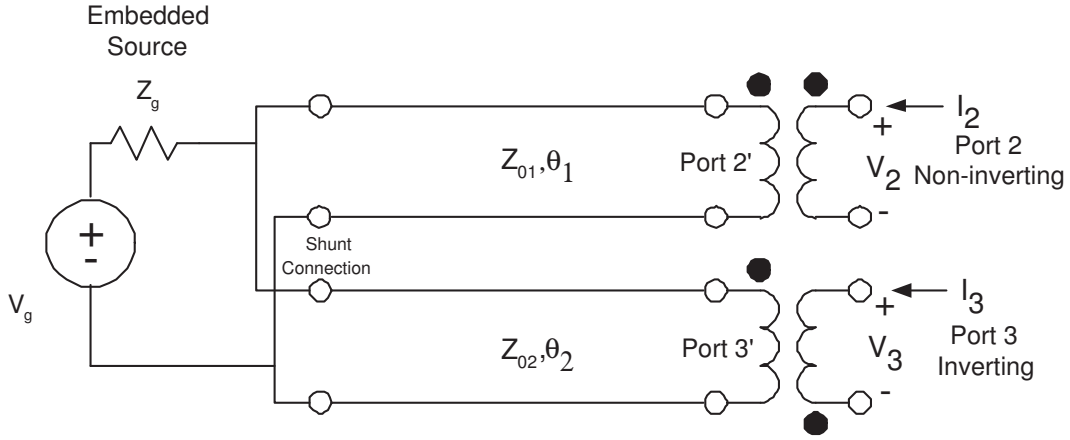


Figure 5: Thévenin Equivalent Model for 3-port consisting of unmatched splitter and invertin transformer.

3' and port 3 as shown in Fig. 5, the impedance parameters become:

$$Z_{22} = Z'_{22}, \quad (4)$$

$$Z_{33} = Z'_{33}, \text{ and} \quad (5)$$

$$Z_{23} = Z_{32} = -Z'_{23}. \quad (6)$$

That is, the phase-inverting transformer inverts  $V_3$  and  $I_3$  thus leaving the diagonal (self) impedance matrix elements unchanged, while changing the sign of the off-diagonal (transfer) elements. The circuit elements in Fig. 4 can be immediately derived from the impedance parameters:

$$Z_A = Z_{22} - Z_{23}, \quad (7)$$

$$Z_B = Z_{23}, \text{ and} \quad (8)$$

$$Z_C = Z_{33} - Z_{23}. \quad (9)$$

As can be seen, all three of these equivalent T network elements are affected by the presence of the phase-inverting transformer. Thus, the Thévenin 2-port equivalent source consists of

the following component impedances and independent source voltages:

$$Z_A = Z_{01} \frac{Y_{01} - Y_{02} \tan \theta_1 \tan \theta_2 + jY_g \tan \theta_1 + Y_{01} \sec \theta_1 \sec \theta_2}{Y_g + jY_{02} \tan \theta_2 + jY_{01} \tan \theta_1}, \quad (10)$$

$$Z_B = -\frac{\sec \theta_1 \sec \theta_2}{Y_g + jY_{01} \tan \theta_1 + jY_{02} \tan \theta_2}, \quad (11)$$

$$Z_C = Z_{02} \frac{Y_{02} - Y_{01} \tan \theta_2 \tan \theta_1 + jY_g \tan \theta_2 + Y_{02} \sec \theta_1 \sec \theta_2}{Y_g + jY_{01} \tan \theta_1 + jY_{02} \tan \theta_2}, \quad (12)$$

$$V_{2OC} = \frac{V_g Y_g \sec \theta_1}{Y_g + jY_{01} \tan \theta_1 + jY_{02} \tan \theta_2}, \text{ and} \quad (13)$$

$$V_{3OC} = -\frac{V_g Y_g \sec \theta_2}{Y_g + jY_{01} \tan \theta_1 + jY_{02} \tan \theta_2}. \quad (14)$$

It is reasonable to consider the special case of equal characteristic impedances,  $Z_{01} = Z_{02} = Z_0 = 2R_g$ , since the characteristic impedance of a coaxial transmission line is a logarithmic function and can typically be very well controlled. Setting  $Z_0 = 2R_g$  provides optimum performance in the equal-delay balun as shown in ref. [8]. In this case, the expressions for the components of the equivalent Thévenin source reduce to:

$$\begin{aligned} Z_A &\rightarrow Z_0 \frac{1 - \tan \theta_1 \tan \theta_2 + j2 \tan \theta_1 + \sec \theta_1 \sec \theta_2}{2 + j \tan \theta_2 + j \tan \theta_1} \\ &= Z_0 \frac{e^{j(\theta_1 + \theta_2)} + j \sin(\theta_1 - \theta_2) + 1}{e^{j(\theta_1 + \theta_2)} + \cos(\theta_1 - \theta_2)}, \end{aligned} \quad (15)$$

$$\begin{aligned} Z_B &\rightarrow -Z_0 \frac{\sec \theta_1 \sec \theta_2}{2 + j \tan \theta_1 + j \tan \theta_2} \\ &= -Z_0 \frac{1}{e^{j(\theta_1 + \theta_2)} + \cos(\theta_1 - \theta_2)} \end{aligned} \quad (16)$$

$$\begin{aligned} Z_C &\rightarrow Z_0 \frac{1 - \tan \theta_2 \tan \theta_1 + j2 \tan \theta_2 + \sec \theta_1 \sec \theta_2}{2 + j \tan \theta_1 + j \tan \theta_2} \\ &= Z_0 \frac{e^{j(\theta_1 + \theta_2)} + j \sin(\theta_2 - \theta_1) + 1}{e^{j(\theta_1 + \theta_2)} + \cos(\theta_1 - \theta_2)}, \end{aligned} \quad (17)$$

$$\begin{aligned} V_{2OC} &\rightarrow V_g \frac{2 \sec \theta_1}{2 + j \tan \theta_1 + j \tan \theta_2} \\ &= V_g \frac{2 \cos \theta_2}{e^{j(\theta_1 + \theta_2)} + \cos(\theta_1 - \theta_2)} \end{aligned} \quad (18)$$

$$\begin{aligned} V_{3OC} &\rightarrow -V_g \frac{2 \sec \theta_2}{2 + j \tan \theta_1 + j \tan \theta_2} \\ &= -V_g \frac{2 \cos \theta_1}{e^{j(\theta_1 + \theta_2)} + \cos(\theta_1 - \theta_2)}. \end{aligned} \quad (19)$$

When the transmission lines are also commensurate ( $\theta_1 = \theta_2 = \theta$ ),  $Z_A$  and  $Z_C$  become frequency independent, but  $Z_B$  does not:

$$Z_A \rightarrow Z_0, \quad (20)$$

$$Z_B \rightarrow -Z_0 \frac{1}{e^{j2\theta} + 1}, \quad (21)$$

$$Z_C \rightarrow Z_0 \quad (22)$$

$$V_{2OC} \rightarrow V_g \frac{2 \cos \theta}{e^{2j\theta} + 1}, \text{ and} \quad (23)$$

$$V_{3OC} \rightarrow -V_g \frac{2 \cos \theta}{e^{2j\theta} + 1}. \quad (24)$$

It was noted in [3] that the 4-port equal-delay hybrid is not truly frequency independent. Here it can be seen that the 3-port balun does not provide frequency independent behavior either, in that the Thévenin equivalent network is frequency dependent even in the ideal, commensurate case. It is useful to notice that when the line lengths are negligible, the source configuration is identical to that associated with a voltage balun as shown in [11]. However, when the line length is  $90^\circ$ , the balun behaves as a current balun, at least in the sense that  $Z_B \rightarrow \infty$ .

Fig. 6 depicts the magnitude of DM and CM voltages across the generalized load in Fig. 3 under three special conditions: (1)  $Z_{DM} = 200 \Omega$  and  $Z_{CM} = \text{open circuit}$ , (2)  $Z_{DM} = 200 \Omega$  and  $Z_{CM} = 50 \Omega$ , and (3)  $Z_{DM} = 200 \Omega$  and  $Z_{CM} = 250 \Omega$ . Thus, case (1) corresponds to  $Y_A^\Delta = Y_C^\Delta = 0$  and  $Y_B^\Delta = \frac{1}{200} \text{ S}$ ; case (2) corresponds to  $Y_A^\Delta = Y_C^\Delta = \frac{1}{100} \text{ S}$  and  $Y_B^\Delta = 0$ ; and case (3) corresponds to  $Y_A^\Delta = Y_C^\Delta = \frac{1}{500} \text{ S}$  and  $Y_B^\Delta = \frac{1}{250} \text{ S}$ . If the load behaves as an isolated 2-terminal impedance (case 1), the behavior would be as described in [5] with perfect nulls occurring at the odd integer multiples of the average quarter-wave frequency. In Fig. 6, it would appear that the CM voltage becomes large for the isolated load when the average electrical length is an odd integer multiple of one-quarter wavelength. However, no power is transferred to the load since in this case the CM impedance is an open circuit.

It is worthwhile to compare this Thévenin equivalent network with that of a feed network consisting of an *ideal* hybrid and two non-commensurate coaxial transmission lines. That is, consider the system with the shunt coaxial splitter replaced by a hybrid network. In this case, the Thévenin equivalent network would simply consist of two isolated independent sources each with a section of transmission line between the source and output. Thus, the two sources are decoupled by the isolating behavior of the hybrid. (Note that an equal-delay hybrid implemented with non-commensurate transmission lines would not exhibit perfect isolation.) The extent to which the behavior of this source differs from that of

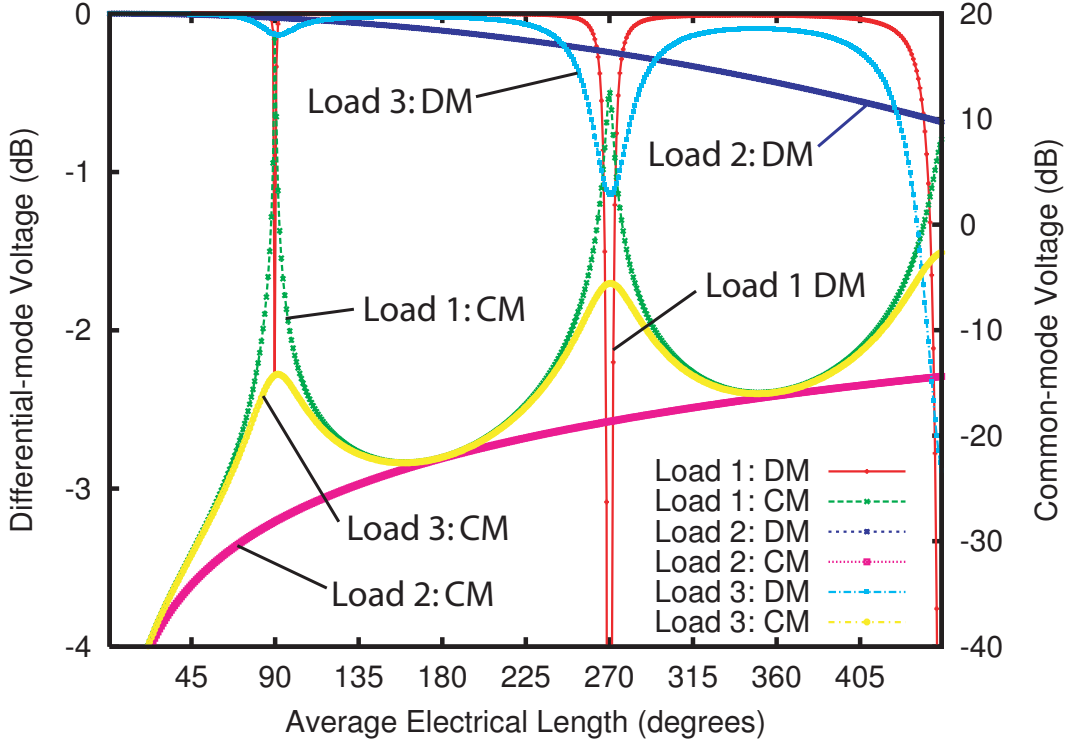


Figure 6: CM and DM Voltages produced by Non-commensurate Balun with  $\pm 5\%$  physical length difference in constituent transmission lines. The characteristic impedances of the lines are equal with  $Y_{01} = Y_{02} = Y_g/2$ .

the above described source depends strongly on the nature of the 2-terminal load to which it is connected. Thus, the remainder (the external structure) of the IRA comes into play. The hybrid coupler decouples the sources at the near (source) end. When the load configuration in Fig. 3 consists as in case (2) of only the two shunt admittances to ground,  $Y_A$  and  $Y_C$ , the two lines are decoupled at the load. Under these ideal conditions, coupling at the source end cannot cause an anomaly. Only when coupling at both ends occurs can these anomalies occur.

### 2.3 Equivalent Common-mode Structure of the IRA

The 2-port, 3-terminal load in Fig. 3 representing the IRA would, in the most general case, be an asymmetric network with  $Y_A^\Delta \neq Y_C^\Delta$ . This is because a slight asymmetry is introduced by the series connection in the feed network. Here we are primarily concerned with the symmetric approximation to the general case. That is, we will consider the antenna to be symmetric but the balun to be non-commensurate and hence asymmetric. In this case the excitation and load can be considered as composed of differential mode (DM) and common-mode (CM) components. At low frequencies the CM impedance would tend

asymptotically to  $Z_{CM} \rightarrow \frac{R_L}{4} = 56.25 \Omega$  where  $R_L$  is the terminating resistance for each of the four transmission line conductors. Because of its symmetry, the IRA excited in the common mode should exhibit a radiation null on its principal axis. The pattern has been computed using a commercial FEM simulation. In very general terms, the CM excitation is similar to a quadrupole composed of two loop currents driven out of phase. Thus, if the antenna bore-sight is aligned with the  $z$  axis, the feed is aligned with the  $x$ -axis so the co-polarization of the antenna on the bore-sight is in the  $x$  direction, then the maximum CM radiation should be in the  $x$  direction as shown in Fig. 7. This is a typical low frequency CM pattern (100 MHz) where the constituent loop currents are electrically small. Of course, this pattern becomes much more complex as the antenna becomes electrically large. The DM and CM impedances of a typical IRA, the Farr Research model IRA-3M, have been computed using a commercial finite element simulation and are presented in Fig. 8. As can be seen, this 2-port,3-terminal load is quite different from an isolated impedance. The CM input impedance tends asymptotically to 56.25 Ohms as the frequency approaches zero. Near 140 MHz, the common mode exhibits a damped series resonance. Near 310 MHz, the common mode structure exhibits a damped parallel resonance. With the exception of the frequency region near this parallel resonance, the driving point impedance for the common mode at the feed point is very small. It will be seen that very little power is transferred to the common mode.

Given the numerically determined values for the differential and common mode impedances of the IRA, it is possible to compute the proportions of the available source power converted into differential and common modes in the antenna structure. It should be remembered that this power is not the radiated power, but rather the power in differential and common modes at the feed point. In the case of both the differential and common mode, some of the power is dissipated in the loads located at the bases of the four feed arms. Referring to Fig. 9, the impedance matrix of the passive network portion of the Thévenin equivalent representation of the balun and signal source is:

$$[Z] = \begin{bmatrix} Z_{11} & Z_{12} \\ Z_{21} & Z_{22} \end{bmatrix}. \quad (25)$$

The impedance matrix of the 2-port antenna model is:

$$[Z_L] = \begin{bmatrix} Z_{11L} & Z_{12L} \\ Z_{21L} & Z_{22L} \end{bmatrix}. \quad (26)$$

It is more straightforward to use a T/Y equivalent network to represent the antenna here.

These are related to the network elements in Fig. 3 by the Y- $\Delta$  transformation:  $Z_{AL} = \frac{Y_A^\Delta}{Y_A^\Delta Y_B^\Delta + Y_B^\Delta Y_C^\Delta + Y_C^\Delta Y_A^\Delta}$ ,  $Z_{BL} = \frac{Y_B^\Delta}{Y_A^\Delta Y_B^\Delta + Y_B^\Delta Y_C^\Delta + Y_C^\Delta Y_A^\Delta}$ ,  $Z_{CL} = \frac{Y_C^\Delta}{Y_A^\Delta Y_B^\Delta + Y_B^\Delta Y_C^\Delta + Y_C^\Delta Y_A^\Delta}$ . The “L” subscript is used to distinguish the components of this network from their counterparts in the equivalent network of the balun/source. In terms of the “T” network elements in Fig. 9, the elements of the impedance matrix are given by:

$$Z_{11L} = Z_{AL} + Z_{BL}, \quad (27)$$

$$Z_{12L} = Z_{BL}, \quad (28)$$

$$Z_{21L} = Z_{BL}, \text{ and} \quad (29)$$

$$Z_{22L} = Z_{CL} + Z_{BL}. \quad (30)$$

These elements in turn, are derived from the computed common and differential mode impedances plotted in Fig. 8:

$$Z_{AL} = \frac{Z_{DM}}{2}, \quad (31)$$

$$Z_{BL} = Z_{CM} - \frac{Z_{DM}}{4}, \text{ and} \quad (32)$$

$$Z_{CL} = \frac{Z_{DM}}{2}. \quad (33)$$

Now, we can write:

$$(Z_{11} + Z_{11L}) I_{1L} + (Z_{12} + Z_{12L}) I_{2L} = V_{1OC} \quad (34)$$

$$(Z_{21} + Z_{21L}) I_{1L} + (Z_{22} + Z_{22L}) I_{2L} = V_{2OC}. \quad (35)$$

These equations can be solved simultaneously for  $I_{1L}$  and  $I_{2L}$ . The differential mode voltages and currents are then:

$$V_{DM} = V_{1L} - V_{2L}, \text{ and} \quad (36)$$

$$I_{DM} = \frac{I_{1L} - I_{2L}}{2}. \quad (37)$$

The common mode voltages and currents are then:

$$V_{CM} = \frac{V_{1L} + V_{2L}}{2}, \text{ and} \quad (38)$$

$$I_{CM} = I_{1L} + I_{2L}. \quad (39)$$

The differential mode power is:

$$P_{DM} = V_{DM}I_{DM}^*. \quad (40)$$

The common mode power is:

$$P_{CM} = V_{CM}I_{CM}^*. \quad (41)$$

In Fig. 10, the fraction of the available source power carried by each mode is plotted. It should be kept in mind that these are the differential and common modes associated with the feed structure, not the radiated power. Some of this power is delivered to the loads at the base of the feed structure. In particular, most of the common-mode power is dissipated by the loads. The average quarter-wave frequency of the the constituent transmission lines is about 120 MHz. As can be seen from Fig. 10, the maximum common mode power for the frequency range examined here occurs near the average three-quarter wave frequency of the constituent transmission lines.

### **3 Numerical Simulation of Representative IRA with Non-commensurate Balun.**

From the data concerning the percentage of power transferred to the differential and common modes plotted in Fig. 10, it is apparent that, for the frequency range examined here, the greatest departure from ideal operation occurs near the average 3/4 wavelength frequency of the constituent transmission lines. This is approximately 357.4 MHz for the IRA considered here which corresponds (roughly) to the Farr IRA-3M. Ideally  $V_A = 1$  V and  $V_C = -1$ V;  $Z_A = 100$  Ohms,  $Z_C = 100$  Ohms, and  $Z_B = -50$  Ohms (Voltage Balun representation). Now consider a non-commensurate balun with  $\pm 5\%$  physical line length difference. Element values for an average electrical length of 270 degrees (357.4 MHz) were computed. This degree of disparity results in the following component values for the

numerical source model:

$$V_A = -4.284 \text{ V}, \quad (42)$$

$$V_C = -4.284 \text{ V (Note signs for voltage sources)}, \quad (43)$$

$$Z_A = 416.53j \text{ Ohms}, \quad (44)$$

$$Z_C = -416.53j \text{ Ohms, and} \quad (45)$$

$$Z_B = 917.49 \text{ Ohms (T network is anti-symmetric)}. \quad (46)$$

At first glance, these values might seem unusual, or perhaps incorrect. For example the independent source voltages appear to represent pure common-mode excitation. Some explanation is warranted. Consider the expression for the independent source voltage in Eqns. 18 and 19 evaluated at an integer multiple of the average quarter-wave frequency:

$$V_{2OC} \rightarrow V_g \frac{2 \cos \theta_1}{e^{2j\theta_{avg}} + 1}, \text{ and} \quad (47)$$

$$V_{3OC} \rightarrow -V_g \frac{2 \cos \theta_2}{e^{2j\theta_{avg}} + 1}. \quad (48)$$

Since in order to be at an integer multiple of the average quarter-wave frequency, the values  $\theta_1$  and  $\theta_2$  are symmetrically situated about a zero of the cosine function and thus  $\cos \theta_1 = -\cos \theta_2$ . Therefore,  $V_{2OC} = V_{3OC}$ . Perhaps it should be kept in mind that the elements of the equivalent network do not each alone correspond to a physical component or phenomenon. The anti-symmetric nature of  $Z_A$  and  $Z_C$  results in the flow of differential mode current and hence power. In fact, as can be seen from Fig. 10, much more power is delivered to the differential more than is delivered to the common mode even at the average three-quarter wave frequency.

A numerical simulation of an IRA with a non-commensurate balun was carried out for a representative model of the Farr IRA-3M using these 2-port Thévenin equivalent source values. The far-field co- and cross-polarization Ludwig-3[12] components are plotted in Fig. 11. Specifically, the quantity that is plotted is:

$$R \left| \vec{E}(R, \theta, \phi) \cdot \hat{a}_{co} \right| \text{ for co-polarization, and} \quad (49)$$

$$R \left| \vec{E}(R, \theta, \phi) \cdot \hat{a}_{cross} \right| \text{ for cross-polarization} \quad (50)$$

where

$$\hat{a}_{co} = \hat{a}_\theta \cos \phi - \hat{a}_\phi \sin \theta, \quad (51)$$

$$\hat{a}_{cross} = \hat{a}_\theta \sin \phi + \hat{a}_\phi \cos \theta, \quad (52)$$

and  $\vec{E}(R, \theta, \phi)$  is the far-field radiated electric field. Since only the far field is being considered  $R \cdot \vec{E}(R, \theta, \phi)$  is independent of  $R$ . As can be seen, even for this degree of disparity in the electrical lengths of the constituent transmission lines, the cross polarization rejection is approximately 30 dB.

## 4 Experimental Investigation of Common-mode Radiation

We have carried out preliminary measurements of the characteristics of a commercially-available IRA in order to support the thesis that the equal-delay feed topology is the source of some anomalous behavior. Fig. 14 depicts a time-domain-reflectometer (TDR) characterization of the reflection coefficient at the input port of the antenna. As can be seen from the cursors, the round-trip time between the small reflection at the shunt splitter and that at the series connection is about 4.2 nanoseconds. Thus, the equivalent air-line distance between these two points is 629.58mm giving a quarter-wave frequency of 119.13 MHz. In Fig. 15, it can be seen that this is reflected (slightly) in the return loss of the system. Periodic peaks in the response on and off axis are apparent in the vicinity of 120 and 240 MHz and to a lesser extent near 480 MHz. These peaks are due in part simply to impedance mismatch within the IRA. While this preliminary data is not calibrated gain data but rather simply insertion loss data, the other antenna is known to have a relatively flat gain over this frequency range. It is clear that the peak in the off-axis response in the vicinity of 240 MHz is greater than that of the on-axis response. The PxM pattern still provides some gain even at 90° off of the main axis and the peak is undoubtedly due in part to impedance mismatch. However, impedance mismatch cannot account for the frequency variation being greater off axis than on axis. Clearly some excitation of the common mode exists.

## 5 Conclusions

We have examined in some detail the effects of non-commensurate constituent transmission lines in the equal-delay balun on the performance of the impulse radiating antenna. While the two constituent transmission lines may be made very similar to one another, it is never possible to make them identical in length and thus, such an investigation is warranted. The

generalized Thévenin equivalent network proposed here for the source should be useful in more comprehensive numerical simulations of the IRA and also provides physical insight to the operation of the equal-delay balancing feed. Also, the approach can be applied to the analysis other antennas using other types of numerical models.

The equal-delay balun exhibits anomalies in its behavior at odd integer multiples of the average quarter-wave frequency of the two constituent transmission lines. The anomalies consist of peaks in the common-mode and dips in the differential mode power transfer. Thus, a non-commensurate balun should cause the IRA to exhibit peaks in common-mode radiation near these frequencies. However, it must be conceded that, even in the case of highly non-commensurate transmission lines, the numerical model predicts little common mode radiation. Moreover, the spurious CM radiation from the commercially-available IRA antenna is so small as to be difficult to measure. Moreover, the most visible anomalies occur below the published lower limit of the antennas operating frequency range. There are several specific reasons for this behavior:

1. The impedance match into the common mode is very poor.
2. The radiation efficiency of the common mode is very low; most of the common mode power is dissipated in the loads.
3. The common mode exhibits a radiation null on the bore-sight of the antenna.

## References

- [1] C. E. Baum, E. G. Farr, and D. V. Giri, "Review of impulse radiating antennas," in *Review of Radio Science, 1996-1999*, W. S. Stone, Ed. Oxford: Oxford University Press, 1999, ch. 12.
- [2] C. E. Baum, "Some characteristics of electric and magnetic dipole antennas for radiating transient pulses," in *Sensor and Simulation Notes*, ser. SSN 125. U. S. Air Force Weapons Laboratory, 1971.
- [3] J. S. McLean, "Analysis of the equal-delay topology for transformers and hybrid networks," *IEEE Trans. Electromagn. Compat.*, vol. 48, pp. 516–521, Aug. 2006.
- [4] C. E. Baum, "Configurations of TEM feed for an IRA," in *Sensor and Simulation Notes*, ser. SSN 0327. U. S. Air Force Weapons Laboratory, 1991.

- [5] J. S. McLean, "Analysis of the equal-delay transformer topology with non-commensurate constituent transmission lines," submitted to *IEEE Trans. Electromagn. Compat.*, 2006.
- [6] J. S. McLean and R. Sutton, "The rigorous of an impulse radiating antenna with a non-ideal feed structure," 2007 EMC Zurich Symposium, Munich, Sept., 2007.
- [7] J. S. McLean, "Balancing networks for symmetric antennas—I: Classification and fundamental operation," *IEEE Trans. Electromagn. Compat.*, vol. 44, pp. 503–514, Nov. 2002.
- [8] E. W. E. Sabin, E. O. Schoenke, *HF Radio Systems & Circuits*. Atlanta: Noble Publishing Corp., 1998.
- [9] H. J. Carlin and A. B. Giordano, *Network Theory: An Introduction to Reciprocal and Nonreciprocal Circuits*. Englewood Cliffs, N.J.: Prentice-Hall, Inc., 1964.
- [10] J. S. McLean, "The rigorous representation of a shielded 3-port balun in the simulation of an antenna system," submitted to *IEEE Trans. Electromagn. Compat.*, 2006.
- [11] —, "Balancing networks for symmetric antennas—II: Practical implementation and modeling," *IEEE Trans. Electromagn. Compat.*, vol. 46, pp. 24–32, Feb. 2004.
- [12] A. C. Ludwig, "The definition of cross polarization," *IEEE Trans. Antennas Propagat.*, vol. 21, pp. 116–119, Jan. 1973.

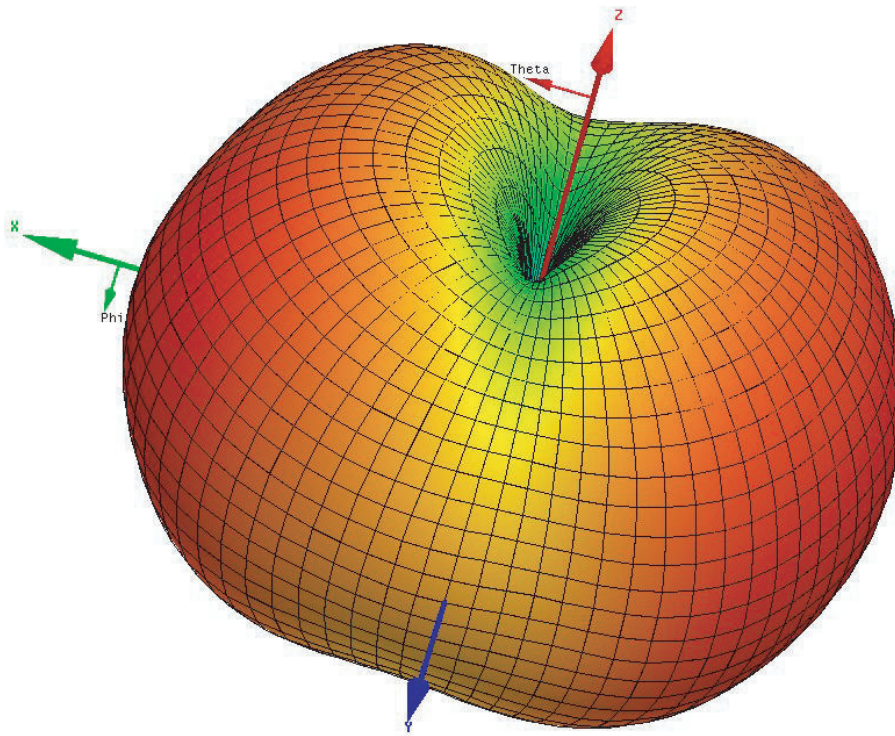


Figure 7: Rendition of the numerically-simulated (with the HFSS finite element simulation program) CM far-field radiation pattern of IRA at 100 MHz. The numerical model is intended to represent an IRA similar to the Farr Research model IRA-3M, although certain simplifications were employed in developing the solid model. The null in the far-field on the bore-sight is clearly visible, however other features of the pattern are somewhat obfuscated by the rendering. It can be seen that the maximum radiation intensity is in the direction of the positive and negative  $x$ -axes as would be expected of the quadrupolar configuration of two loops driven out of phase. Nulls does not exist on the  $y$ -axes as would for true quadrupole radiation, but the radiation intensity is significantly smaller in the  $y$  direction than it is in the  $x$  direction.

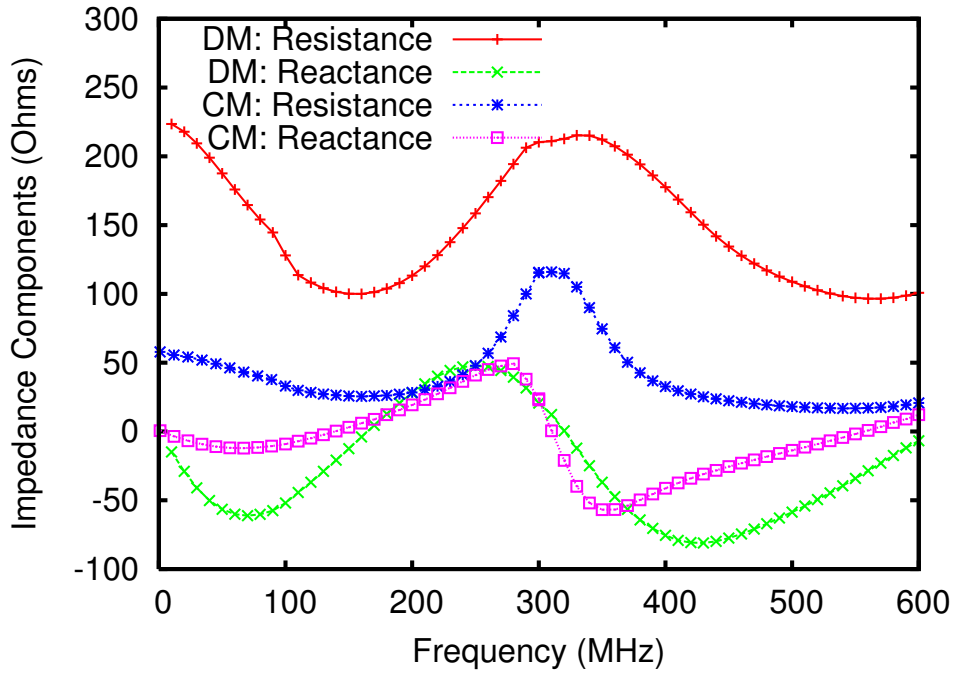


Figure 8: Numerically simulated input impedance at feed point (the junction between the balun and the four feed arms at the focus of the reflector) for equivalent common and differential mode structures. The CM input impedance tends asymptotically to  $\frac{450}{8} = 56.25$  Ohms as the frequency approaches zero while the differential mode input impedance tends asymptotically to  $\frac{450}{2} = 225.0$  Ohms as the frequency approaches zero.

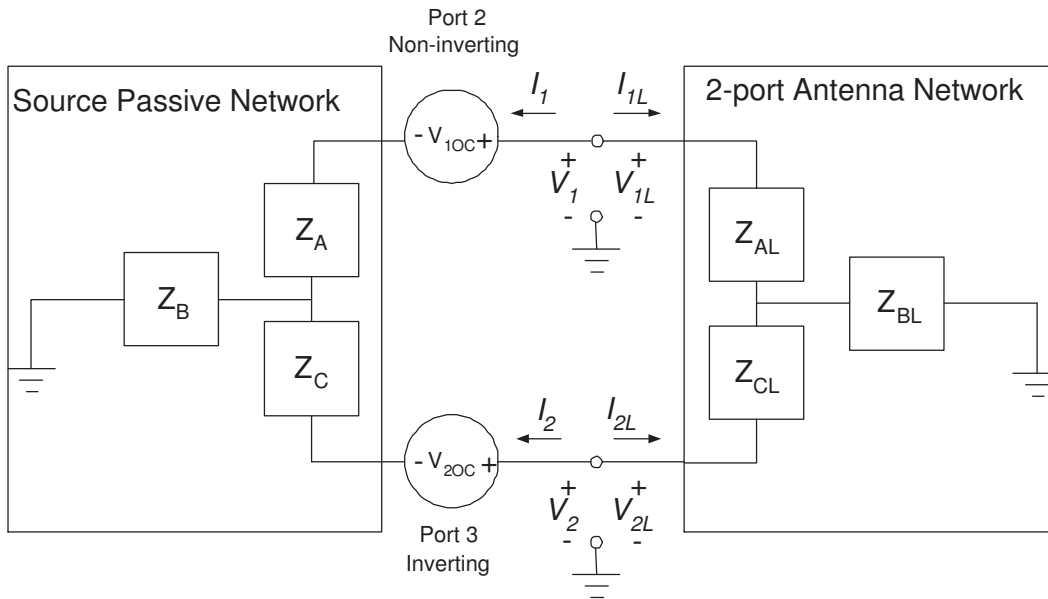


Figure 9: Network connection of 3-port balun model and 2-port antenna model.

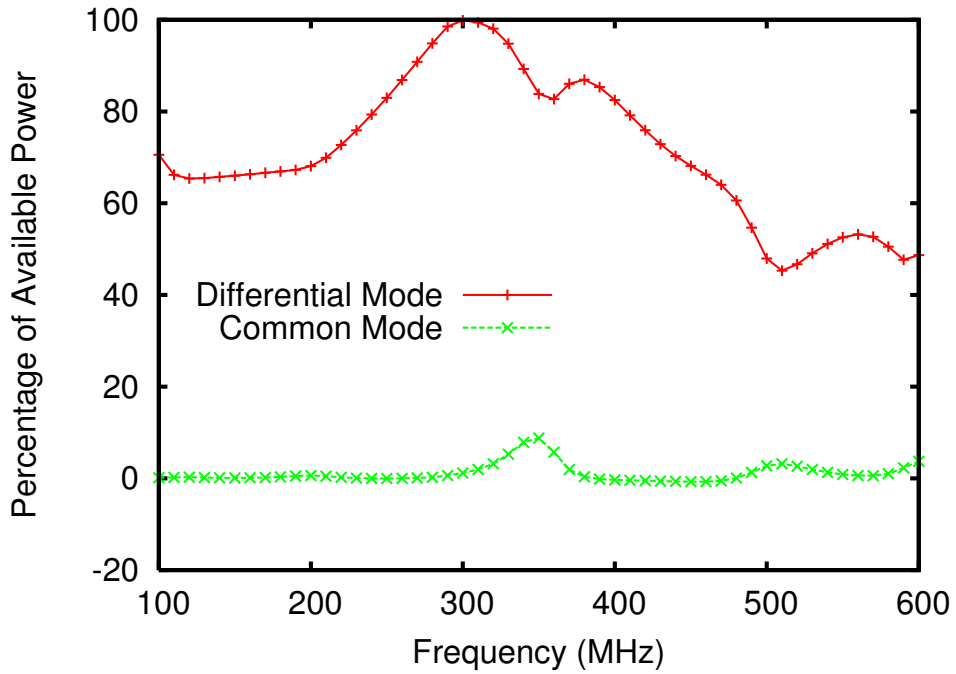


Figure 10: Fraction of available source power carried by differential and common modes. Note that these are modes of the feed system, not radiated power. Some of the power in each mode is delivered to the loads. In particular, most of the common-mode power is dissipated in the loads.

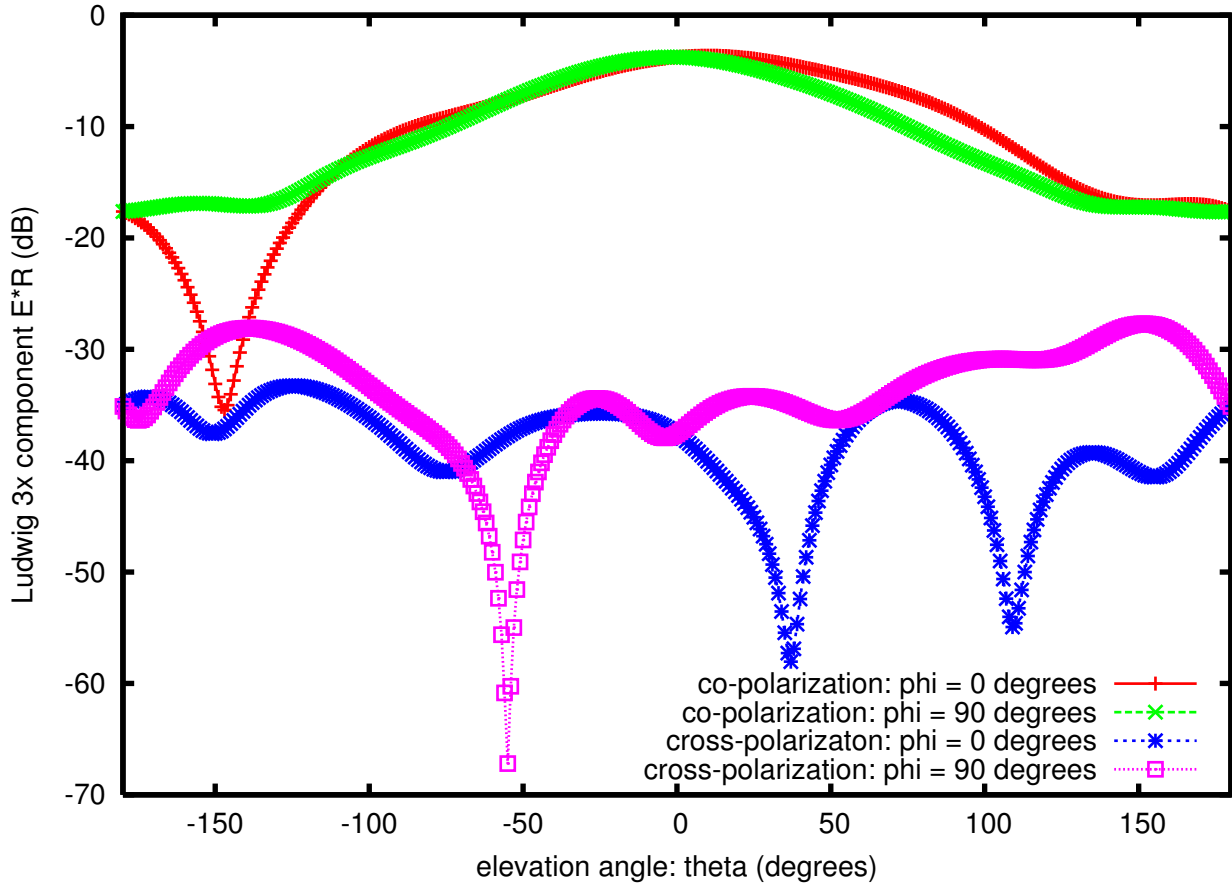


Figure 11: Principal plane radiation patterns for the co- and cross-components of the Ludwig-3 polarization decomposition. The  $y$  axis is the Ludwig-3 [12] electric field component multiplied by the radial distance  $R$  and normalized to 1 Volt.

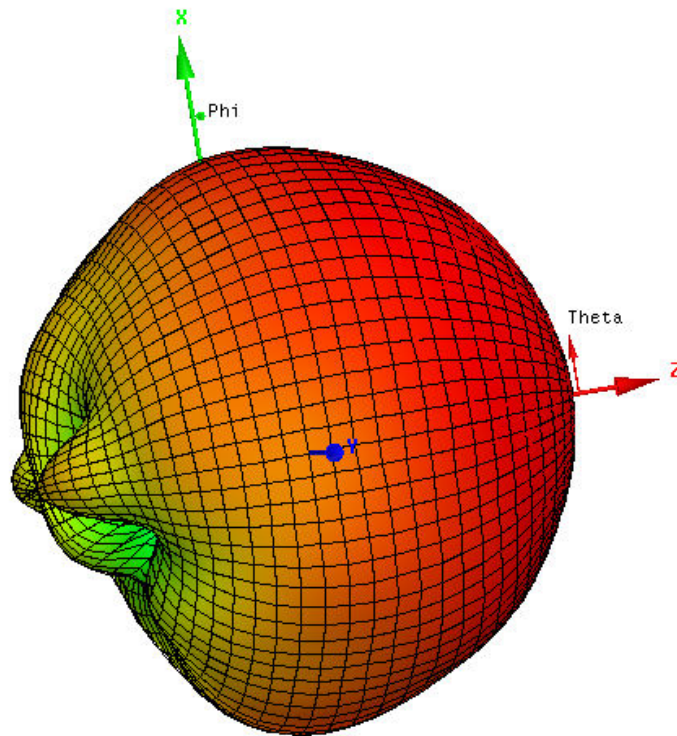


Figure 12: Rendition of the numerically-simulated (with the HFSS finite element simulation program) far-field Ludwig-3 co-polarized component of the radiation pattern of IRA at 360 MHz. The IRA geometry corresponds to the Farr Research model IRA-3M with a  $\pm 5\%$  disparity in the electrical lengths of the constituent transmission lines of the feed structure. It can be seen that the maximum radiation intensity is in the  $z$  direction.

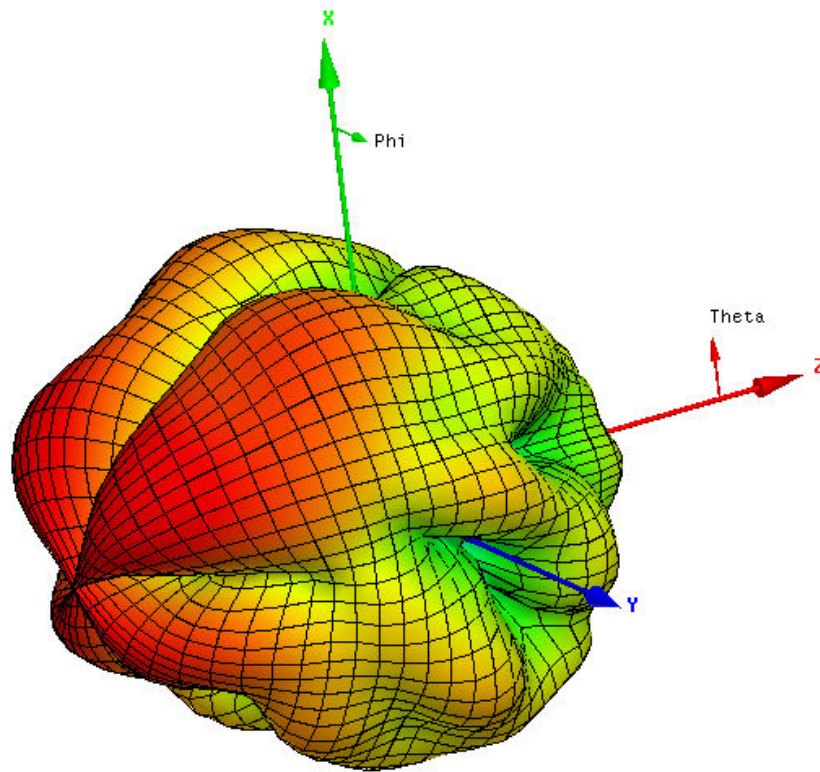


Figure 13: Rendition of the numerically-simulated (with the HFSS finite element simulation program) far-field Ludwig-3 cross-polarized component of the radiation pattern of IRA at 360 MHz. The IRA geometry corresponds to the Farr Research model IRA-3M with a  $\pm 5\%$  disparity in the electrical lengths of the constituent transmission lines of the feed structure. It can be seen that the radiation intensity the  $z$  direction is very small compared to that generally in the back lobe.

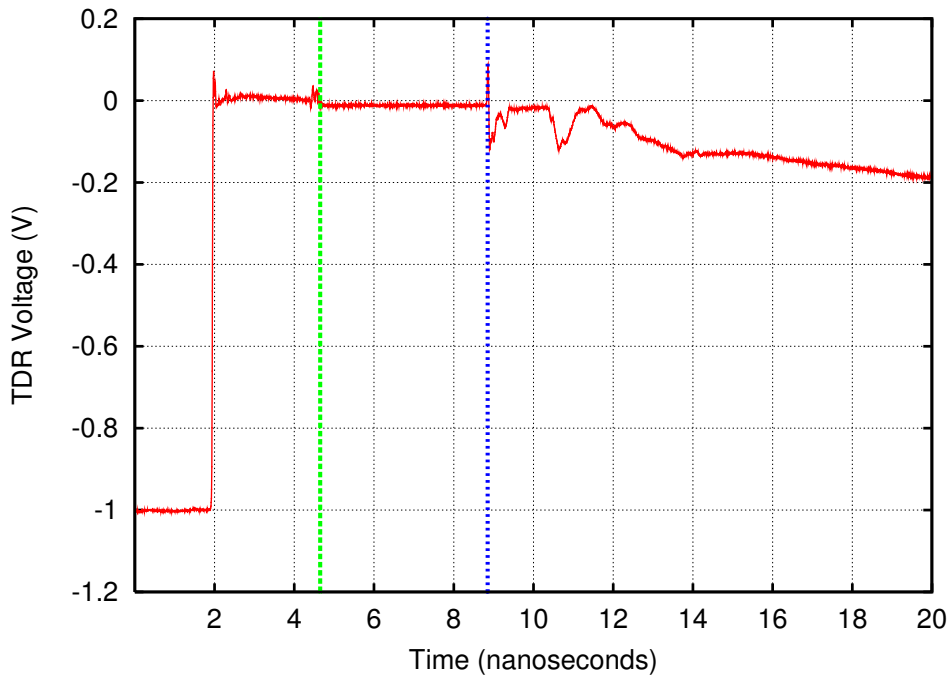


Figure 14: TDR for input of IRA. The green cursor indicates the reflection caused by the shunt splitter; the blue cursor indicates the reflection at the series connection; the interval is 2.1 nanoseconds. The corresponding quarter-wave and half-wave frequencies are approximately 120 and 240 MHz.

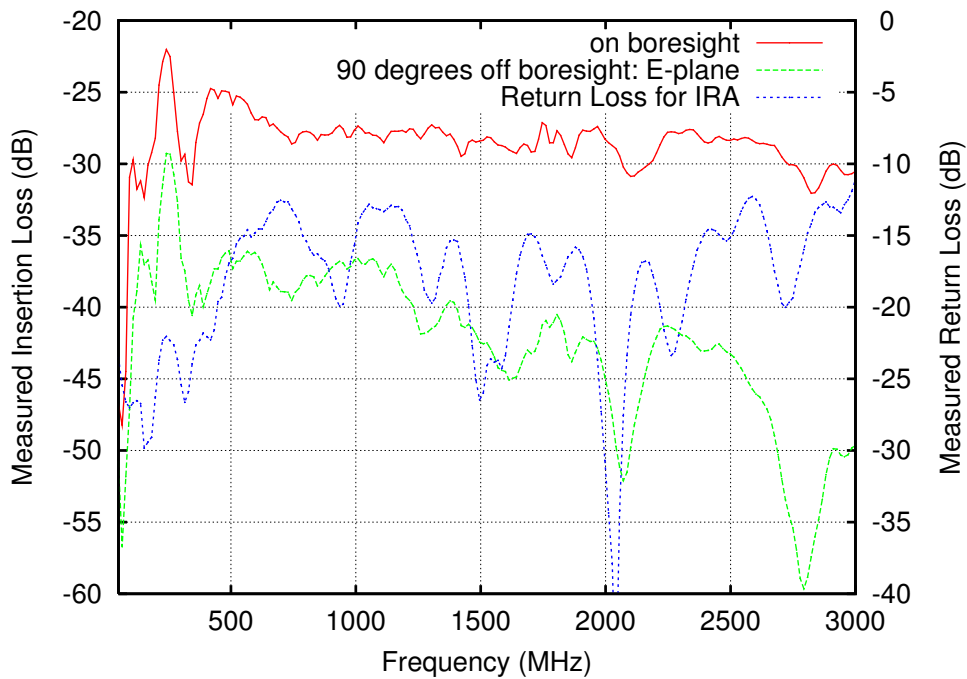


Figure 15: Insertion loss measured between IRA and LPDA augmented with broadband dipole